Crustal deformation across the western Altyn Tagh fault (86° E) from GPS and InSAR

Yanchuan Li, Jean-Mathieu Nocquet, Xinjian Shan

Geophysical Journal International

Geophys. J. Int. (2022) **228,** 1361–1372
Advance Access publication 2021 October 05
GJI Geodynamics and tectonics

https://doi.org/10.1093/gji/ggab403

Crustal deformation across the western Altyn Tagh fault (86° E) from GPS and InSAR

Yanchuan Li [1,2] Jean-Mathieu Nocquet [1] and Xinjian Shan[2]

[1] *Geoazur, IRD, CNRS, Observatoire de la Côte d'Azur, Université Côte d'Azur, Valbonne 06905, France. E-mail: yanliupcc@gmail.com*
[2] *State Key Laboratory of Earthquake Dynamics, Institute of Geology, China Earthquake Administration, Beijing 100029, China*

Accepted 2021 September 30. Received 2021 September 28; in original form 2020 November 6

SUMMARY

We combine Global Positioning System (GPS) velocity field with Interferometric Synthetic Aperture Radar (InSAR) results to study the interseismic deformation across the western Altyn Tagh fault (ATF) at longitude 86° E. GPS and InSAR data are consistent after correcting for the contribution from vertical deformation in the InSAR line-of-sight map. InSAR and GPS data identify an area of ∼2 mm a^{-1} sinistral shear and ∼6 mm a^{-1} of NS shortening located ∼150 km south of the ATF near the Manyi fault system. Excluding the data located in that area, Bayesian inversion of a 2-D profile across the ATF indicate a locking depth of 14.8 ± 3.5 km and a slip rate of 8.0 ± 0.4 mm a^{-1}, lying at the lower range of previously published estimates. In addition, we find no significant offset between the fault at depth and the surface fault trace and no asymmetry of the interseismic profile that implicitly reveal lateral variations of the elastic strength across the ATF. Detailed analysis of InSAR profile across the fault show no distinguishable surface creep along the western ATF. Our study highlights how different data sets, data selection and model assumption might impact results on the ATF slip rate, locking depth and rheological contrast across the fault.

Key words: Satellite geodesy; Asia; Continental tectonics: strike-slip and transform.

1. INTRODUCTION

The ∼1600 km long Altyn Tagh fault (ATF) is one of the major continental-scale faults in Asia, which separates the Tibetan Plateau from the weakly deformed Tarim basin. The ATF defines a major boundary accommodating the eastward motion of the Tibetan Plateau (e.g. Molnar & Tapponnier 1975; Fig. 1) and its slip rate has been a matter of debate to discriminate among continental deformation models (e.g. Bendick *et al*. 2000; Wright *et al*. 2004a; Chevalier *et al*. 2011).

During the last 20 yr, Global Positioning System (GPS) measurements have been used to estimate the slip rate of the ATF (e.g. Bendick *et al*. 2000; Shen *et al*. 2001; Wallace *et al*. 2004; Zhang *et al*. 2004; Zhang *et al*. 2007; He *et al*. 2013; Li *et al*. 2018) with estimates ranging from 8 to 10 mm a^{-1}. In addition, Interferometric Synthetic Aperture Radar (InSAR) has provided constraints with higher spatial resolution on the relative motion across the fault. However, an inherent limitation of InSAR measurement is that it only provides the component in the satellite line of sight (LOS) of the 3-D velocity field (e.g. Wright *et al*. 2004a; Elliott *et al*. 2008; Jolivet *et al*. 2008; Zhu *et al*. 2016; Daout *et al*. 2018; Liu *et al*. 2018; Xu & Zhu 2019). Neglecting the vertical deformation present in the LOS map may impact the fault slip rate estimates. The relatively dense GPS sites across the western ATF (86° E; He *et al*. 2013), together with InSAR measurements spanning the 2003–2011 period (Daout *et al*. 2018), provides a chance to investigate how potential vertical deformation in LOS may impact the fault slip rate estimation, and to improve the robustness and accuracy of the 3-D crustal motion across the fault.

Aside the slip rate and locking depth estimates, asymmetry in the interseismic strain across the ATF has been reported. It has been interpreted as being induced either by a rigidity contrast within the upper crust across the fault (e.g. Elliott *et al*. 2008; Jolivet *et al*. 2008), or a dislocation shift at depth relative to the surface fault trace (e.g. Vernant 2015), implicitly implying a dip angle of 45° for the ATF, a model at odds with geomorphic observation (e.g. Molnar *et al*. 1987).

Recently, Xu & Zhu (2019) processed InSAR data spanning the 1996–2017 period across the western ATF (83° E–86° E; Fig. S1, Supporting Information). They propose ∼2.0 mm a^{-1} of surface creep extending to 1.0–2.0 km depth along the 300-km-long fault segment.

In this study, we take advantage of horizontal GPS velocity field and InSAR results covering the same area across the ATF to re-evaluate any potential technique and model biases. After a careful analysis and data selection, we propose a robust estimate of the slip rate, locking depth and asymmetry profile across the ATF. In addition, we probe the presence of surface creep at the western ATF.

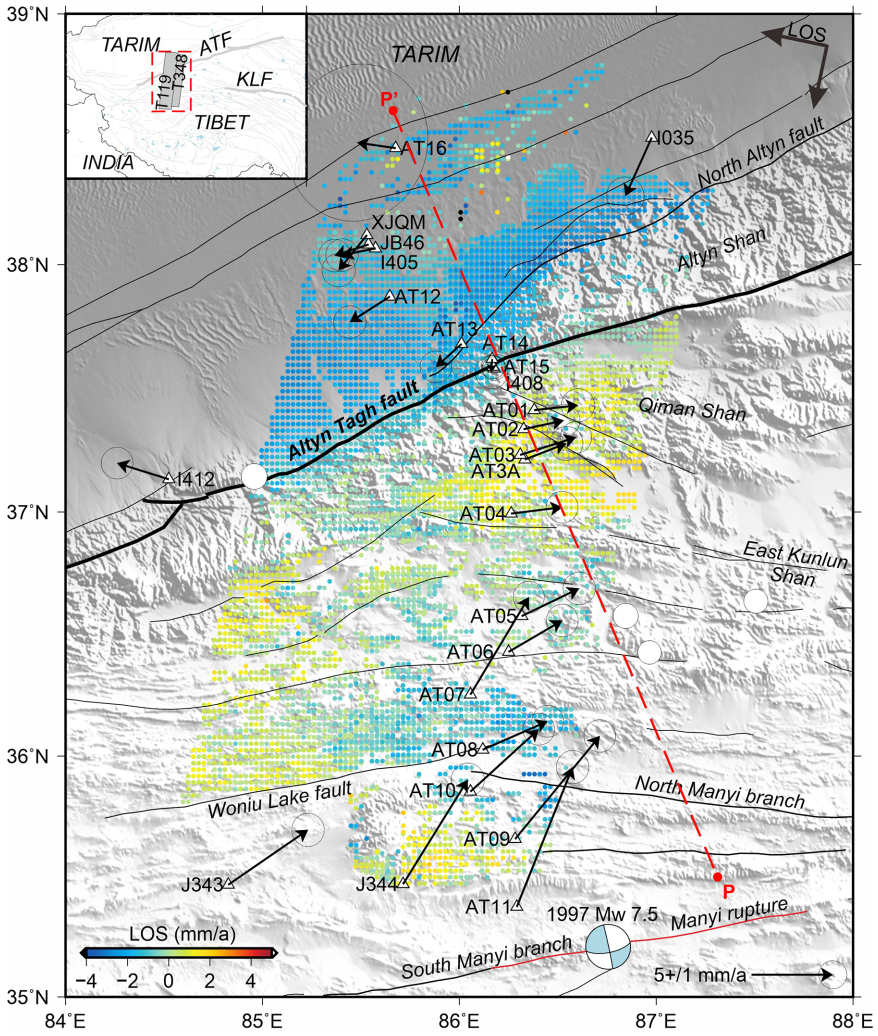

Figure 1. Active tectonic map of the northwestern Tibetan Plateau and geodetic results. White triangles indicate the location of GPS sites, with site names labelled (see He et al. [2013] for details). Black arrows show GPS velocities referenced to the AT15 site with error ellipses at the 67 per cent (1σ) confidence level. InSAR data are from Daout *et al*. (2018), here downsampled for clarity (see the main text). Black lines indicate crustal faults that are come from Seismic Active Fault Survey Data Center (http://www.activefault-datacenter.cn/). The light blue focal mechanism solution (Global Centroid Moment Tensor, GCMT) shows the 1997 M_w 7.5 Manyi earthquake, with red solid line represents the surface rupture (Funning *et al*. 2007). White circles represent earthquakes with magnitudes between 5 and 6 from 2009 to 2017 (U.S. Geological Survey, USGS). The red dashed line indicates the position of the velocity profile. Inset shows the location of study area and InSAR frames. ATF: Altyn Tagh fault and KLF: Kunlun fault.

2. GEODETIC DATA

2.1 GPS data

We used 17 GPS benchmarks crossing the western ATF (86° E; Fig. 1). The first two-to-three campaigns of measurement were conducted He *et al*. (2013) between 2009 and 2013. In October 2017, we conducted another campaign of measurements of the same benchmarks. We used these three campaigns of data in this work. Processing details are explained fully in He *et al*. (2013). In this study, velocity uncertainties are derived using the 'realistic sigma' algorithm (Herring *et al*. 2016) while simple least squares were used in Li *et al*. (2018). More details are described in Supporting Text S1 and GPS position time-series are shown in Fig. S2 in the Supporting Information.

2.2 InSAR data

InSAR data used in this study are from Daout *et al*. (2018). Four Environmental Satellite (Envisat) descending tracks (T348, T119, T391 and T162; Fig. S1, Supporting Information) covering the northwestern Tibetan Plateau between 2003 and 2011 were processed using the New Small Baselines Subset chain (Doin *et al*. 2011, 2015) based on the ROI_PAC software (Rosen *et al*. 2004). During the processing, atmospheric delays, effects of hydrology and permafrost seasonal changes in the high plateau and orbital residuals were corrected. Fig. 1 shows the LOS rate map (T348 and T119) across the western ATF, with warm colours represent motion towards the satellite and cold colours away from the satellite, consistent with the left-lateral motion across the ATF. InSAR points are downsampled from the original data of Daout *et al*. (2018) and

drawn in a 'low resolution' for clarity, with a spatial sampling of ∼2.8 km (Fig. 1). The downsampled data are used in our subsequent 2-D modelling to reduce computational burden. When using the InSAR data to derive fault creep rate (Section 3.6), we instead use the original undecimated data (T348, T119, T391 and T162), which have a resolution of ∼40 m.

3. GEODETIC DATA ANALYSES

3.1 GPS velocity field

We first compare the GPS velocity solution between 2009 and 2011 from He *et al*. (2013; Fig. 2a) with the results for the 2009–2017 period (Fig. 2b). In overall, the two velocity solutions show a good agreement in magnitude and direction. Due to the limited campaigns of measurement, it's hard to assess the impact of seasonal variations on GPS site velocity (Blewitt & Lavalée 2002). Nonetheless, in the Supporting Information (Text S2), we show that the seasonal variations can affect GPS site velocity at a level of 1.5 mm a^{-1}.

To highlight the strain pattern across the ATF, the GPS velocities (2009–2017) are transformed relative to the AT15 site, which is located ∼200 m south of the fault trace (Fig. 1). GPS velocities show a clear decrease towards the fault and have opposite directions across fault, consistent with the left-lateral motion along the ATF. While gradual changes in site velocities are observed south of AT01, a sharp change in velocities between AT01 and AT13 (40 km apart) suggests the region probably accommodates most of the interseismic strain.

For further analysis, GPS velocities are projected into their components perpendicular and parallel to the fault (Fig. 3). The profile is centred on the fault trace (86.1741° E, 37.5836° N) and normal to the ATF (Fig. 1). The fault-perpendicular velocities show ∼0.3 mm a^{-1} shortening rate over a 250 km wide region (AT08–XJQM; Fig. 3a). To the southern end of the profile, we find ∼2 mm a^{-1} of sinistral shear and ∼6 mm a^{-1} shortening between AT11 and AT10 (Fig. 3a), ∼150 km away from the ATF. That area corresponding to the Manyi fault system, which has been proposed to be a potential boundary accommodating the relative motion of the Qaidam block to the north and the West Qiangtang block to the south (e.g. Loveless & Meade 2011; Wang *et al*. 2017). Previous elastic block models predict shortening rates from 3 to 8 mm a^{-1}, an amount consistent with the motion of AT11, AT09, J344 and AT10 with respect to the sites located north of the North Manyi branch (Fig. 1). Moreover, InSAR LOS velocities show a ∼1–2 mm a^{-1} changes across the western end of the North Manyi branch (Daout *et al* . 2018), which may extend farther west and coincident with the Woniu Lake fault, a secondary strike-slip fault of the Manyi system. Therefore, we exclude GPS sites AT11, AT09, J344 and AT10 in our subsequent modelling. The velocity for site AT07 is an obvious outlier when compared to its neighboring sites AT06 and AT08 (Fig. 1). It is also excluded from our model.

3.2 Alignment of GPS and InSAR

In order to investigate potential vertical deformation contribution to the InSAR LOS map, we compare the GPS horizontal velocities with the LOS displacements from tracks 348 and 119 (Fig. 1). As the GPS and InSAR data are referenced to different frames, the first step is to remove the offset between different frames. For each GPS site, we calculate the dispersion of the InSAR LOS values for pixels located within a circle radius of 1–10 km. We select three GPS stations (AT13, AT14 and AT15), for which the dispersion of the colocated LOS values is stable and small (root mean square less than 0.4 mm a^{-1}; Fig. S3, Supporting Information) to align the two data sets. Horizontal velocities of these three GPS sites are projected onto the LOS according to local incidence angles ($LOS^{GPS}_{AT13} = 0.48$ mm a^{-1}, $LOS^{GPS}_{AT14} = -0.06$ mm a^{-1} and $LOS^{GPS}_{AT15} = 0$ mm a^{-1}). Then we estimate a mean InSAR LOS rate inside a circle with 1 km radius ($LOS^{InSAR}_{AT13} = 1.89$ mm a^{-1}, $LOS^{InSAR}_{AT14} = 1.12$ mm a^{-1} and $LOS^{InSAR}_{AT15} = 1.04$ mm a^{-1}). Finally, the averaged value (1.21 mm a^{-1}) of offsets between LOS^{GPS} and LOS^{InSAR} is subtracted from all the InSAR observations.

The alignment of GPS and InSAR allows us to quantify the contribution of vertical deformation to LOS under the assumption of negligible relative vertical motion among the three reference GPS sites. To verify the assumption, horizontal velocities of AT13, AT14, AT15 and AT12 are projected onto LOS and compared with InSAR observations (Fig. S4, Supporting Information). The good consistency between LOS projections and observations suggests no obvious relative vertical motion between AT13/AT14/AT15 and AT12, the latter of which is located in the Tarim basin and is experiencing minimal vertical motion (0 to -0.2 ± 1.04 mm a^{-1}; Liang *et al*. 2013). Therefore, the derived vertical motion in the following could be simply regarded as referenced to the Tarim basin. Hereafter, unless otherwise specified, GPS and InSAR are in the same reference frame, that is, InSAR refers to data after the reference frame translation described above. Other specific corrections for InSAR data are explained in the following and each figure caption.

3.3 Correction of the geodetic data for block rotation

The cross-fault GPS velocities are shown in Fig. 3(a). We note that the fault-parallel component to north of the ATF shows a systematic trend away from the fault. We suspect that this trend, which is seen far away from the ATF, might be related to the block rotation on a profile rather than a consequence of actual strain rate. In order to test this hypothesis, we use the Euler poles from Wang *et al*. (2017) for the Tarim (longitude of 96.80 ± 0.21° E, latitude of 38.49 ± 0.05° N and rotation rate of -0.689 ± 0.009°Ma^{-1}) and West Qiangtang (longitude of 120.13 ± 3.74° E, latitude of 11.49 ± 5.20° N and rotation rate of -0.167 ± 0.028°Ma^{-1}) blocks to calculate the fault-parallel and fault-perpendicular components induced by block rotations (Fig. S5, Supporting Information). Results show that to the south of the ATF, block rotation contributes ∼0.3 mm yr^{-1} to the fault-parallel and ∼0.1 mm a^{-1} to the fault-perpendicular velocities along the ∼160-km-long profile, which are negligible compared with the GPS velocity uncertainty (0.4 mm a^{-1}). However, north of the ATF, the rotating block results in ∼1.3 mm a^{-1} fault-parallel gradient and <0.1 mm a^{-1} to the fault-perpendicular velocities over the ∼100-km-long profile, which would bias the ATF slip rate estimate. Consequently, we correct the block rotation for the GPS velocities to the north of the fault and obtain a corrected fault-parallel velocity profile (Fig. 3b).

3.4 Separation of vertical deformation in InSAR LOS data

For the NEE strike-slip ATF, LOS displacement is more sensitive to the vertical deformation than horizontal deformation (Wright *et al*. 2004b). It is therefore critical to correct any potential vertical

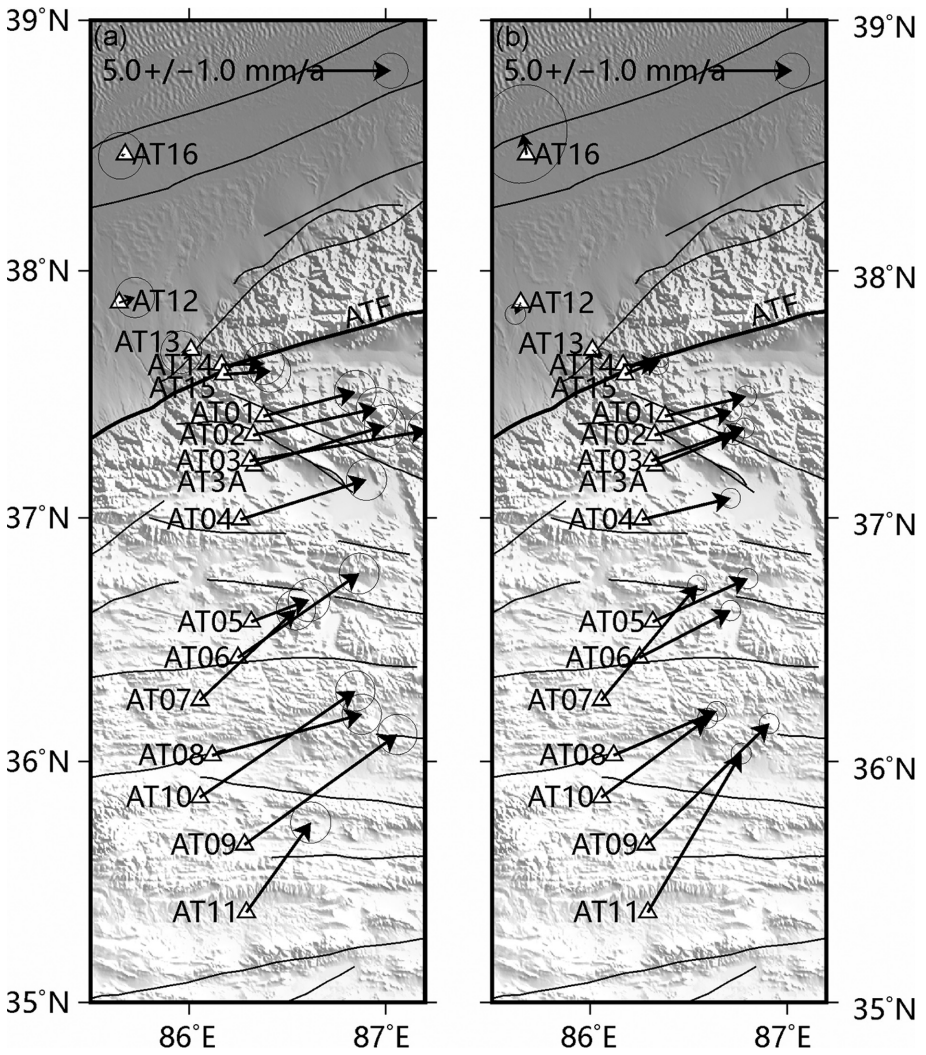

Figure 2. GPS velocities for sites across the western ATF from (a) 2009–2011 (He *et al*. 2013) and (b) 2009–2017. All GPS velocities are under a Tarim-fixed reference frame, with uncertainties at the 67 per cent confidence level. Note that the 2009–2017 solution was the result of a new campaign of measurement based on the 2009–2011 observations of He et al. (2013). See section 2.1 for details.

velocity in the InSAR LOS. No leveling measurement has been implemented across the western ATF, and only the descending InSAR data are available for the moment. Thus, we quantify the vertical deformation from a direct comparison of GPS and InSAR. We first use a 2-D model (presented in Section 3.5) to fit the fault-parallel GPS velocities and obtain the optimal dislocation parameters (slip rate, locking depth and dislocation location shift) of the ATF. Using the obtained dislocation parameters, we then calculate the fault-parallel velocities at each InSAR point. Finally, we project the fault-parallel velocities onto the LOS and compare with the InSAR observations (Fig. 4). Using this procedure, the differences between the predicted LOS rates and the observations should be mainly related to vertical motion. The vertical velocity map shows several regions with notable uplift and one region with subsidence (Fig. 4c). The deformation rates are larger than the LOS uncertainty ($\sim$1.0 mm a^{-1}), suggesting the vertical deformation should be significant. Consequently, InSAR points located in those regions are masked out in the following 2-D models.

Following the procedure of block rotation correction for GPS site velocities, we correct the block rotation contributions from InSAR data to the north of the ATF (Fig. 3b). Analyses of the vertical deformation as well as its contribution to the fault parameter inversions are presented in the discussion section.

3.5 2-D dislocation modelling

At this step, selected/corrected GPS and InSAR points (Sections 3.1, 3.3 and 3.4, Fig. 3b) are used for dislocation modelling. The western ATF is modelled as a buried infinite screw dislocation in an elastic half-space, where the left-lateral aseismic slip occurs at a rate of V_0 below a locking depth of D. A horizontal dislocation shift (d) from the fault trace is introduced to account for the possible geodetic data asymmetry across the fault. For a displacement $V(x)$ at a perpendicular distance x from the fault, $V\ (x) = (V_0/\pi)\ * \arctan((x-d)/D) + a$ (Savage & Burford 1973), a is a velocity constant over the studied area. We use a Bayesian approach to derive the posterior probability density function (PDF) of the model parameters (Minson *et al*. 2013; Nocquet 2018). The posterior PDF $p(\boldsymbol{m}|\boldsymbol{d})$ is defined as: $p(\boldsymbol{md}) \sim p(\boldsymbol{m})\exp[(\boldsymbol{d}-\boldsymbol{r})^T C^{-1}(\boldsymbol{d}-\boldsymbol{r})]$, where $\boldsymbol{d}$ and $\boldsymbol{r}$ are vectors containing the observations and model predictions, C^{-1} is the inverse of the covariance matrix of the data and $p(\boldsymbol{m})$ is the prior

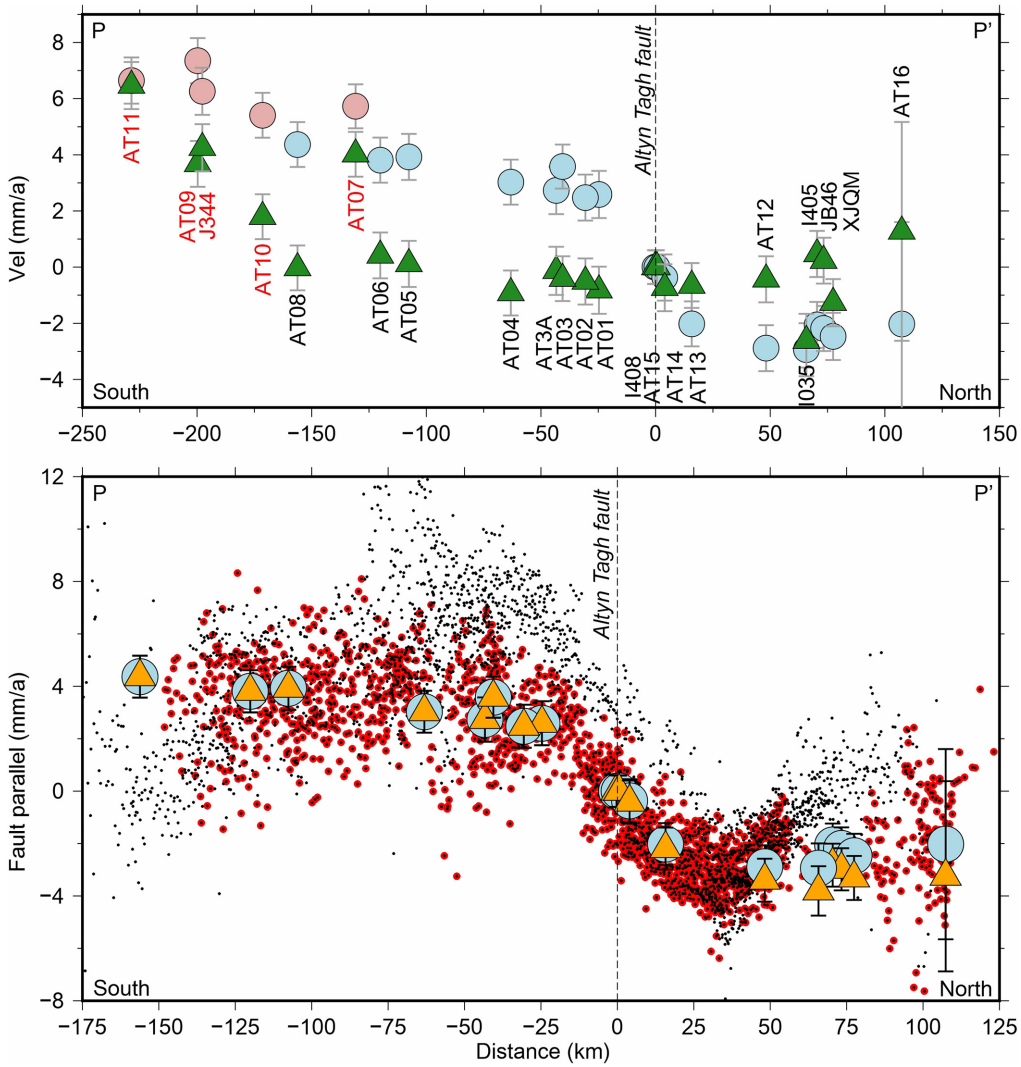

Figure 3. Geodetic profiles across the ATF. Top: circles and triangles are fault-parallel (NE positive) and fault-perpendicular (NW positive) components respectively. Pink circles with red labels are GPS sites that are excluded from our 2-D modelling. Error bars show 1σ uncertainties. Bottom: fault-parallel components of GPS velocities across the western ATF before (circles) and after (triangles) the correction for the contribution from the Tarim block rotation. Dots show InSAR before (black) and after (red) masking out points in the localized uplift and subsidence regions. InSAR data have been aligned to the GPS reference frame, then corrected for the contribution from the Tarim block rotation, and finally projected to the fault-parallel direction. The InSAR point locations are shown in Fig. 1. Origin of x-axis corresponds to surface trace of the ATF.

PDF of the model parameters. We use uniform prior distributions and construct the covariance matrix as diagonal matrix using the GPS and InSAR data uncertainties. Results presented below are derived from a total of 10 000 sampling from the Markov chain.

Inversion results using GPS only, InSAR only and both data are shown in Table 1. The GPS only model shows a strike-slip rate of 8.6 $\pm$ 0.8 mm a^{-1} and a locking depth of 22.0 $\pm$ 7.1 km along the western ATF (Fig. 5a). The InSAR only model shows a fault slip rate and locking depth of 8.0 $\pm$ 0.6 mm a^{-1} and 13.5 $\pm$ 4.1 km, respectively (Fig. 5b). Joint inversion of GPS and InSAR data results in smaller parameter uncertainties, with slip rate estimated at 8.0 $\pm$ 0.4 mm a^{-1} and fault locking depth at 14.8 $\pm$ 3.5 km (Fig. 5c). Using the optimal fault locking depth and dislocation offset (0.6 $\pm$ 1.5 km to the south), the dip angle of the ATF is estimated to be $\sim$87°, which agrees with fault structure from magnetotelluric data interpretations (e.g. Zhang *et al*. 2015; Xiao *et al*. 2017). Because the GPS sites are relatively sparsely distributed (0–25 km) in the near-field of the fault, the improvement for GPS-InSAR inversion is significant with respect to the GPS-only model. Our slip rate estimate shows overall consistency with that found in previous studies (e.g. Elliott *et al*. 2008; He *et al*. 2013; Vernant 2015; Daout *et al*. 2018; Li *et al*. 2018; Table 2). Discrepancies among dislocation offsets and fault locking depths are discussed below.

3.6 Deriving surface creep rate along the western ATF

We calculate the 'surface creep rate' using InSAR LOS data (T348, T119, T391 and T162; Fig. S1, Supporting Information) with both 'short profile' and 'long profile' methods. In the short profile method, the LOS velocities are taken in small boxes crossing the fault (2 km normal each side of the fault and 2 km along the strike). For each profile, we do a linear regression to fit a straight line at each side of the fault, then calculate the modelled velocity at the points closest to the fault ($x = \pm 0.5$ km). The 'surface creep rate' is estimated by differencing the modelled fault-parallel velocities.

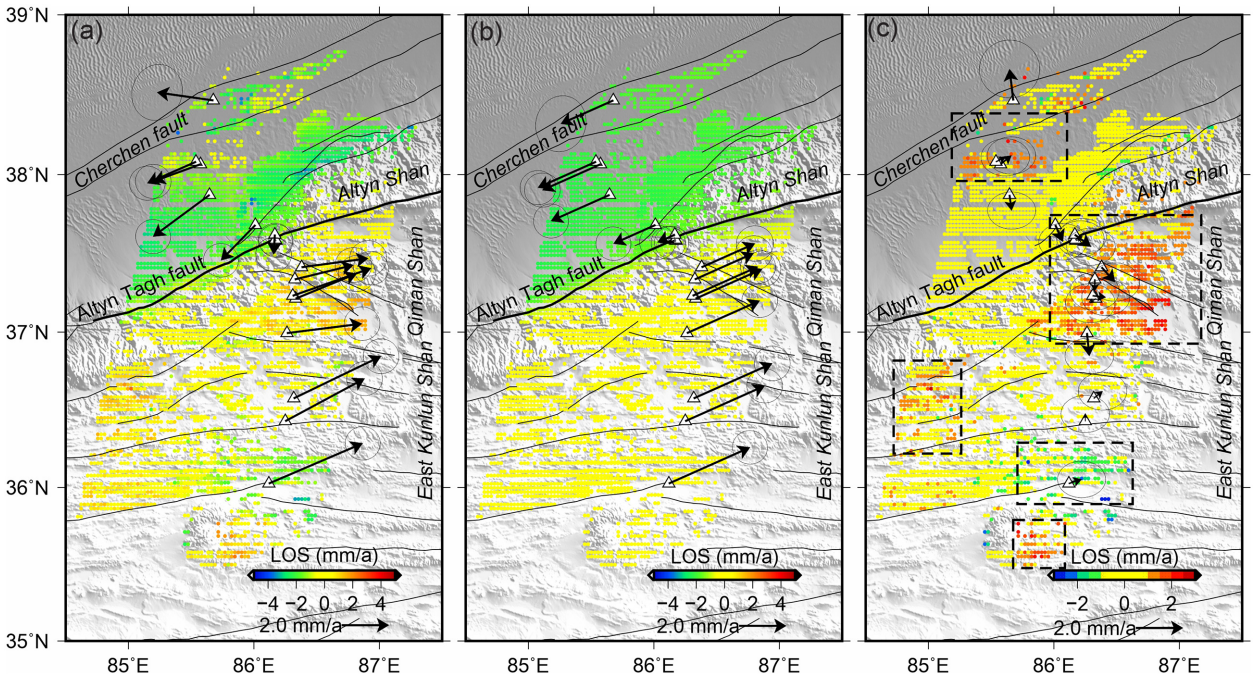

Figure 4. Data, model prediction and residuals. (a) Observed GPS and InSAR data. Both data sets have been corrected for the contribution from the Tarim block rotation and are in the same reference frame. (b) Best model predictions for LOS and horizontal GPS. (c) Residuals (observation-model) GPS and LOS maps. Rectangles outline the area of localized subsidence (cold colour) and uplift regions (warm colour) excluded in our 2-D model.

Table 1. Inversion results of different models.

Slip rate (mm a^{-1})	Locking depth (km)	Dislocation shift to South (km)	Rigidity ratio	Model	Data source
8.6 ± 0.8	22.0 ± 7.1	0.1 ± 2.3	—	Without rigidity	GPS
8.1 ± 1.3	21.7 ± 7.2	0.2 ± 2.4	0.50 ± 0.10	With rigidity	
8.0 ± 0.6	13.5 ± 4.1	2.1 ± 2.4	—	Without rigidity	InSAR
7.8 ± 0.4	13.9 ± 3.6	2.0 ± 2.4	0.47 ± 0.02	With rigidity	
8.0 ± 0.4	14.8 ± 3.5	0.6 ± 1.5	—	Without rigidity	GPS + InSAR
7.6 ± 0.4	15.2 ± 3.6	0.6 ± 1.5	0.48 ± 0.02	With rigidity	

If the fault segment is creeping, the LOS data should show a step across the fault and thus the 'surface creep rate' would be larger than 0. Alternatively, the LOS data would be a smoothed curve across the fault and the 'surface creep rate' should be around 0 within the confidence level.

In the long profile method, cross-fault points are taken in boxes of 100 km normal either side of the fault and 2 km along strike. By adding a second term $(V_c/\pi) * \arctan(d_c/x)$ to the 2-D model in Section 3.5, surface creep rate (V_c) and creep depth (d_c) are estimated simultaneously.

Fig. 6 shows the creep rate estimation results (Fig. S6, Supporting Information shows examples of velocity profile fitting). Despite fluctuations in 'surface creep rate' (< 0.5 mm a^{-1}) along the fault distance, no obvious LOS rate step is identified across the fault, implying tight or fully fault locking at shallow depth. The discrepancies between our results and that of Xu & Zhu (2019) might indicate slip motion along the ATF is variable in both time and space domain. This topic is beyond the scope of this study hence not discussed here.

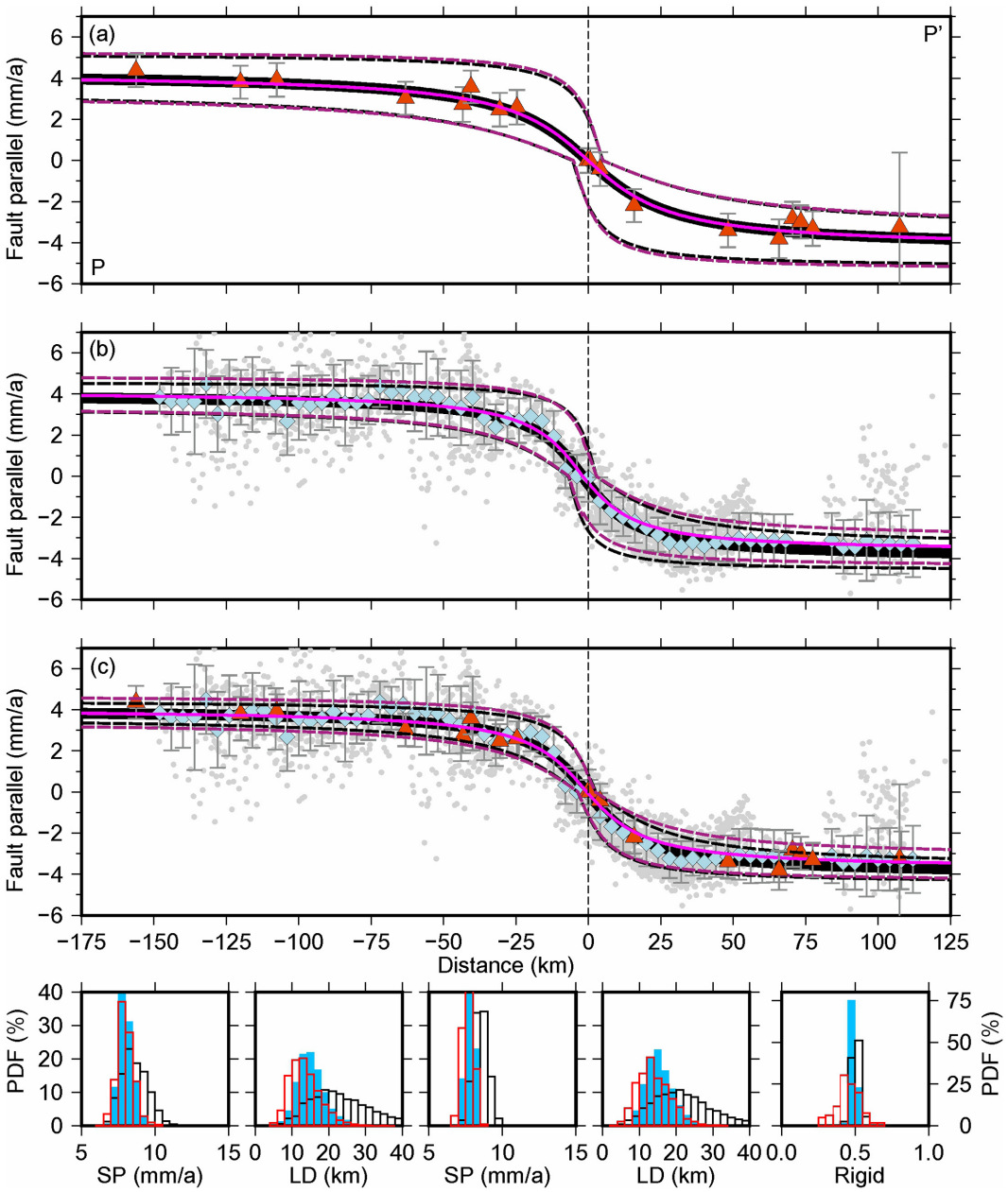

Figure 5. Observed and modelled fault-parallel velocities across the western ATF. Red triangles and light blue diamonds with 1σ uncertainty error bars show the fault-parallel velocity component of the GPS and InSAR respectively. Thick blue solid lines represent best model, without rigidity contrast for (a) GPS data only, (b) InSAR data only and (c) joint inversion of GPS and InSAR. Thick magenta solid lines represent best-fitting curves with the rigidity parameter considered. Thin dotted lines outline 95 per cent confidence levels. The velocity of each InSAR data point is calculated using the median rates and their standard deviation of all the pixels (grey dots) within a 4-km-wide bin along the profile. InSAR data here have been corrected both the contribution of block rotation and localized vertical deformation. The bottom panels show posterior marginal PDFs using GPS data only (black histogram), InSAR data only (red histogram) and GPS + InSAR data (blue histogram). The first two subplots are for a model without rigidity parameter. The three subplots on the right correspond to the model with the rigidity parameter estimated. SP and LD are short for slip rate and locking depth, respectively. Rigid is for the rigidity parameter (see the main text).

4. DISCUSSION

4.1 Factors impacting the ATF slip rate estimate

Our slip rate estimate of the western ATF (86° E) overlaps with the range proposed in previous studies, summarized in Table 2. Here, we emphasize several factors that might impact the slip rate estimation and provide some explanations to the discrepancies found with respect to previous studies. A first factor is the selection of geodetic points. If the southernmost GPS sites (AT11, AT09, J344 and AT10; Fig. 1), which are located in the region of transpressive deformation near the Manyi fault system, are included in the 2-D model, the fault slip rate appears to be overestimated by 35 per cent (10.8 $\pm$ 1.3 mm a^{-1}, Fig. S7a, Supporting Information). A second factors is the impact of possible remaining uplift/subsidence signal in InSAR used for modelling. To investigate this point, we perform an inversion without masking out the InSAR data located in the localized uplift and subsidence regions. The results infer a fault slip rate of 7.5 $\pm$ 0.9 mm a^{-1} only slightly lower than our estimates, but a fault

Table 2. Summary of previous studies crossing the western ATF (86° E).

Slip rate (mm a^{-1})	Locking depth (km)	Dislocation shift to South (km)	Data source	Reference
$9.0^{-3.2}/_{+4.0}$	14.5	13.0	GPS (2009–2011)	He *et al*. (2013)
$8.6^{-3.2}/_{+4.2}$	$14.5^{-14.5}/_{+15.5}$	$12.5^{-13.5}/_{+7.5}$	GPS (2009–2011)	Vernant (2015)
8.1 ± 0.7	13 ± 4	∼20*	GPS (2009–2011)	Zheng *et al*. (2017)
$10.5^{-1.1}/_{+1.0}$	$17.6^{-6.1}/_{+6.9}$	0	GPS (2009–2011)InSAR (2003–2011)	Daout *et al*. (2018)
8.5 ± 1.0	21.3 ± 9.8	0	GPS (2009–2017)	Li *et al*. (2018)
8.0 ± 0.4	14.8 ± 3.5	0.6 ± 1.5	GPS (2009–2017)InSAR (2003–2011)	This study

*This value is only an approximate estimate.

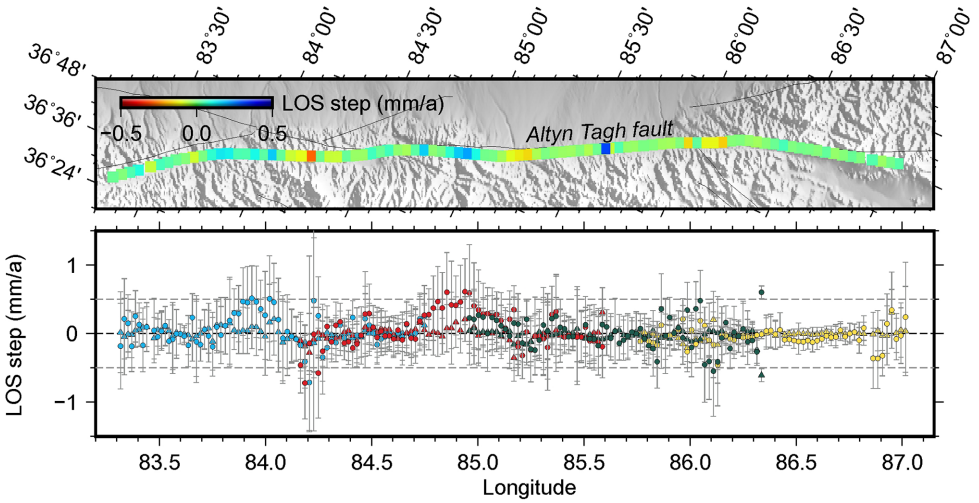

Figure 6. Creep rate calculation results along the western ATF. The upper panel shows LOS step results, from the 'short profile' method (see the main text), overlapping on DEM. The lower panel shows LOS step results as a function of longitude. Circle colours are for different InSAR tracks. Triangles and circles correspond to the 'short profile' and 'long profile' methods, respectively (see explanations in the main text). Error bars show 3σ (99 per cent confidence level) uncertainties.

locking depth of 7.6 ± 6.7 km (Fig. S7b, Supporting Information), about half the locking depth found for our preferred model (Fig. 5c). Such a model also finds a dislocation offset of 5.8 km northwards of the fault, contradictory to what is expected for a more rigid Tarim basin and high dip angle of the ATF (e.g. Zhang *et al*. 2015; Xiao *et al*. 2017).

Secondary faults, not accounted for in our modelling might also impact slip rate estimates. We focus here on the North Altyn fault (Fig. 1), which was identified as a left-lateral transpressive fault with predominant strike-slip motion (e.g. Cowgill *et al*. 2000). The North Altyn fault is oblique to the ATF at longitude 86° E and then runs 30 km away and parallel to the ATF. We simulate the LOS velocity field caused by two strike-slip faults, similar to the ATF and North Altyn faults geometry. We adopt a far-field loading rate of 10 mm a^{-1} and partition the slip between the two faults (Fig. S8, Supporting Information). Because the short separation distance between the two faults, results show that the deformation fields are similar (LOS differences are less than 1 mm a^{-1}), preventing to evaluate a potential slip partitioning between the two faults. We note an LOS velocity gradient across the North Altyn fault, but the sense of LOS change would imply right-lateral motion for the North Altyn fault (Supporting Text S3). Deployment of dense GPS sites and decomposition of InSAR LOS from ascending and descending orbits would help determine the slip rate along the North Altyn fault.

In summary, our tests highlight that slip rate estimates for the ATF are sensitive at 2 mm a^{-1} level to the selection of data. Locking depth estimates are even more sensitive and change by as much as 50 per cent.

4.2 Origin of interseismic strain asymmetry across the western ATF

Asymmetric interseismic strain across strike-slip faults, such as the San Andreas Fault (e.g. Savage *et al*. 2004; Fialko 2006) and the North Anatolian Fault (e.g. Meade *et al*. 2002), has been reported. It is generally interpreted as induced by lateral changes of the elastic thickness (e.g. Chéry 2008), lateral variations in the elastic strength across the fault (Le Pichon *et al*. 2005), or a shift in the position of dislocation at depth relative to the fault trace (Vernant 2015).

Across the eastern segment of ATF (94° E), asymmetric patterns of InSAR velocities are proposed to reflect the effects of a rigidity decrease from Tarim to Qaidam and a southward offset of 5–7 km from the northern ATF to the southern ATF (Zhang *et al*. 2004; Jolivet *et al*. 2008). This interpretation seems to not applicable across the western ATF (85° E, ∼150 km west of our GPS profile). InSAR velocities show a sense of asymmetry ∼10 km to the north of the fault (Elliott *et al*. 2008), opposite to what would

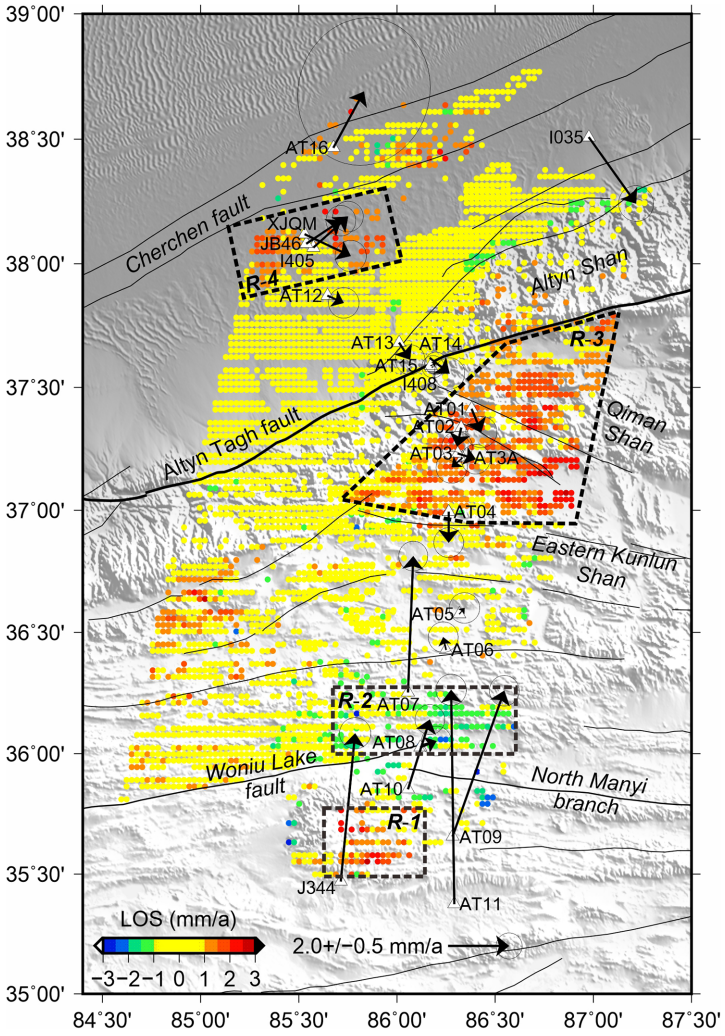

Figure 7. InSAR LOS and GPS residuals. Residuals are observations minus model predictions. Regions defined by the dashed lines represent areas of localized vertical deformation seen in LOS. All GPS velocities have uncertainties at the 95 per cent confidence. Note that this figure indicates no long-wavelength variation in vertical deformation across the ATF.

be expected for a more rigid Tarim Basin or dislocation shift to the south.

Across the ATF at 86° E, previous studies using GPS implicitly suggest asymmetric strain pattern, illustrated by the dislocation shifts of ∼13–20 km, depending on different modeling strategies, to the south of the fault (Vernant 2015; Zheng *et al*. 2017). On the basis of the GPS phase observations of He *et al*. (2013), by adding a new campaign of measurement, our result shows a dislocation shift of 0.6 ± 1.5 km to the south (Fig. 5 and Table 2). In order to identify the factors contributing to the asymmetry velocity pattern across the ATF, we performed several tests. First, we use the GPS velocities in the 2009–2013 period, defined as Model-A. Second, the GPS velocities are the same with Model-A, but the two points (AT09 and AT10) at southern end of the profile are removed. This model is named as Model-B. Third, we use GPS velocities in the 2009–2017 period (points at the southern end of the profile are removed, other sites are the same with Model-B) but do not correct the block rotation contribution. This model is named as Model-C. Finally, GPS points are the same with Model-C but contributions from block rotation are corrected, defined as Model-D. The dislocation offsets (to the south) obtained by Model-A, -B, -C and -D are 14.5 ± 5.0, 10.9 ± 5.9, 5.2 ± 5.8 and 1.3 ± 5.3 km, respectively (Fig. S9, Supporting Information). These tests suggest that differences in the selection of GPS stations (Section 3.1) and model assumption (Section 3.3) could lead to different results related to the question of whether the strain distribution is symmetrical across the fault.

To further test how rigidity contrast within the upper crust across the ATF impacts our results, we invert the geodetic data again for slip rate, locking depth and a rigidity ratio K according to the equations (e.g. Jolivet *et al*. 2008):

$$V\ (x) = \begin{cases} \dfrac{2\mathrm{K}\mathrm{V}_0}{\pi}\arctan\left(\dfrac{\mathrm{x}-\mathrm{d}}{\mathrm{D}}\right) + a, & \text{if } \mathrm{x} > \mathrm{d} \\ \dfrac{2\,(1-\mathrm{K})\,\mathrm{V}_0}{\pi}\arctan\left(\dfrac{\mathrm{x}-\mathrm{d}}{\mathrm{D}}\right) + a, & \text{if } \mathrm{x} < \mathrm{d} \end{cases}$$

where K is the asymmetry coefficient, ranging from 0 to 1. This coefficient represents the rigidity ratio between the upper crust on each side of the fault. A value of K = 0.5 indicates no rigidity contrast between two sides of the fault.

The rigidity contrast between the northern Tibetan Plateau and the southern Tarim basin is estimated to be 0.50 ± 0.10, 0.47 ± 0.02 and 0.48 ± 0.02 from inversions of GPS, InSAR and GPS + InSAR,

respectively (Fig. 5). These results indicate that a rigidity contrast is not required by the geodetic data and that an upper bound of it is 11 per cent for a more rigid Tarim basin compared to the northern Tibetan Plateau. Including a rigidity parameter in the GPS-InSAR inversion leads to values for fault slip rate (7.7 ± 0.4 mm a^{-1}), fault locking depth (15.2 ± 3.6 km) and dislocation offset (0.6 ± 1.5 km) that are consistent with our preferred, simpler model results (Section 3.5).

4.3 Vertical deformation in the northwestern Tibetan Plateau

After correcting for reference frame, for effect of block rotation and for the LOS prediction of our best model for the ATF, the residual InSAR LOS map highlights several regions with unmodelled signal, likely due to vertical deformation (Fig. 4c). Four of them that are covered by GPS sites, allowing to check potential signal consistency for the two data sets. Fig. 7 shows the residual InSAR LOS map, together with the residual GPS velocity field corrected using our 2-D best model for the ATF.

Zone R-1 shows positive 1–2.5 mm yr^{-1} LOS rate, consistent with uplift over a 40×40 km^2 area. Here, residual GPS velocities at sites J344 and AT11 with respect to AT10 and AT09 indicates shortening of ∼3–4 mm yr^{-1} in a roughly NS direction (Fig. 7). The consistency between uplift and shortening seen in our GPS data suggests that this signal is true and has a tectonic origin.

North of R-1 and north of the Woniu Lake fault and North Manyi branch, negative 1–2 mm yr^{-1} LOS rate are found in region R-2. GPS velocities of AT08 and AT07 show a relative extension rate of ∼4 mm a^{-1}, that would be consistent with subsidence. However, AT07 is clearly an outlier with respect to its nearest neighbours AT08 and AT06 and the overall GPS velocity field from the ATF to AT08 (Fig. 1), preventing clear conclusion to be drawn here. At a larger scale, the consistent motion and strain seen for the subset of sites (J344, AT11, AT09 and AT10) with respect to all (except AT07) GPS sites north of latitude 35.8° N, are consistent with a major tectonic boundary accommodating up to 6 mm a^{-1} of shortening and ∼2 mm a^{-1} of left-lateral shear. It is further consistent with the prediction of kinematic models at the scale of the Tibetan Plateau (Loveless & Meade 2011; Wang *et al*. 2017).

Partly adjacent and south of the ATF, a wide area noted R-3 shows positive 1–2.5 mm a^{-1} LOS rates, consistent with uplift. Although only minor crustal shortening (<1 mm a^{-1}) and shear deformation (∼0.2 mm a^{-1}) rates are observed in our GPS velocities (AT04–AT01) across this region, the vertical motion is consistent with that produced by interseismic strain across the Qiman-Kunlun thrusts, in which the Qiman thrust dips to south and is located to the north of the Qiman Shan, and the north dipping Kunlun Shan thrust is located to the south of the Eastern Kunlun Shan.

Finally, positive 1–2 mm a^{-1} LOS rates, consistent with uplift region, is observed north of the ATF, south of the Cherchen fault (Fig. 7, R-4). Our GPS ATF-perpendicular velocities show a roughly ∼0.3 mm a^{-1} contraction rate between AT12 and I405/JB46/XJQM, a magnitude that could partially account for the uplift rate. The flat-ramp model proposed by Daout *et al*. (2018) predicts ∼0.7 mm a^{-1} crustal shortening between ATF and the Cherchen fault also could not fully explain the localized vertical motion.

Taken together, these results suggest that, although the interseismic strain rate appears to be dominated by locking along the ATF, there are secondary contributions of additional active faults. A similar observation has been made by Wright *et al*. (2004a) for instance for an LOS profile across the ATF ∼500 km west of our study. These results call for denser GPS velocity fields, multiple InSAR observations and detailed field investigations to better delineate the complex crustal deformation in the northwestern Tibetan Plateau.

5. CONCLUSIONS

We combine interseismic InSAR data with GPS velocity data across the western ATF (86° E). The geodetic data are consistent after masking out the (InSAR) points located in regions with vertical deformation. Careful selection of the geodetic data and removal of the block rotation contributions from the fault-parallel velocities enable us to robustly estimate the slip rate and locking depth of the western ATF using a simple 2-D elastic dislocation model. A best fit is obtained with a left-lateral strike-slip rate of 8.0 ± 0.4 mm a^{-1} and locking depth of 14.8 ± 3.5 km.

Different from previous studies that implicitly imply a asymmetric GPS velocity pattern, our results indicate no significant asymmetric interseismic velocities across the western ATF. A detailed analysis of InSAR data across the western ATF (83° E–86° E) shows no obvious surface creep implying that the fault is locked all from the surface to the base of the brittle crust.

Our results also show several regions with apparent vertical deformation. GPS velocities indicate overall shortening and extensional crustal deformation in regions of uplift and subsidence, respectively. While further analysis is required to confirm the robustness of uplift and subsiding signals in InSAR data, their origin in terms of tectonics processes might deserve attention in future.

ACKNOWLEDGEMENTS

We are grateful to all people who participated in the GPS fieldwork. The 2009–2011 GPS phase observations were come from He *et al*. (2013), based on which we conducted another campaign of measurement in 2017. We deeply thank Simon Daout and his co-workers for sharing the InSAR results. The first author thanks to Chunyan Qu for her preliminary work of the GPS measurement in 2017, to Wenyu Gong for her discussion on the early draft. Comments and suggestions from Eric Cowgill, Lei Wu, one anonymous reviewer and the editor Kosuke Heki greatly improved the quality of our manuscript. This work was supported by the National Natural Science Foundation of China (grant nos 41631073 and 41461164002). YL was financially supported by the China Earthquake Administration and the China Scholarship Council. All figures were generated using the Generic Mapping Tools (GMT) software (Wessel *et al*. 2013).

DATA AVAILABILITY

GPS velocity solution is accessible in the published paper (He *et al*., 2013). The InSAR LOS solution is available through Daout *et al*. (2018). We used GPS data from seven stations of Crustal Movement Observation Network of China, which were provided by the National Earthquake Infrastructure Service, China Earthquake Administration.

REFERENCES

Bendick, R., Bilham, R., Freymueller, J., Larson, K. & Yin, G., 2000. Geodetic evidence for a low slip rate in the Altyn Tagh fault system, *Nature,* **404**(6773), 69–72.

Blewitt, G. & Lavallée, D., 2002. Effect of annual signals on geodetic velocity, *J. geophys. Res.,* **107**(B7), doi:10.1029/2001JB000570.

Chéry, J. 2008. Geodetic strain across the San Andreas Fault reflects elastic plate thickness variations (rather than fault slip rate), *Earth planet. Sci. Lett.,* **269**(3), 352–365.

Chevalier, M.-L., Li, H., Pan, J., Pei, J., Wu, F., Xu, W., Sun, Z. & Liu, D. 2011. Fast slip-rate along the northern end of the Karakorum fault system, western Tibet, *Geophys. Res. Lett.,* **38,** L22309, doi:10.1029/2011GL049921

Cowgill, E., Yin, A., Wang, X. & Zhang, Q., 2000. Is the North Altyn fault part of a strike-slip duplex along the Altyn Tagh fault system?, *Geology,* **28**(3), 255–258.

Daout, S., Doin, M. P., Peltzer, G., Lasserre, C., Socquet, A., Volat, M. & Sudhaus, H., 2018. Strain partitioning and present-day fault kinematics in NW Tibet from Envisat SAR interferometry, *J. geophys. Res. Solid Earth,* **123**(3), 2462–2483.

Doin, M.-P. *et al.*, 2011. Presentation of the small baseline NSBAS processing chain on a case example: the Etna deformation monitoring from 2003 to 2010 using Envisat data, in *Proceedings of the Fringe Symposium, European Space Agency,* Frascati, Italy, 3434–3437.

Doin, M.-P., Twardzik, C., Ducret, G., Lasserre, C., Guillaso, S. & Jianbao, S.(2015). InSAR measurement of the deformation around Siling Co Lake: inferences on the lower crust viscosity in central Tibet, *J. geophys. Res. Solid Earth,* **120,** 5290–5310.

Elliott, J. R., Biggs, J., Parsons, B. & Wright, T. J., 2008. InSAR slip rate determination on the Altyn Tagh Fault, northern Tibet, in the presence of topographically correlated atmospheric delays, *Geophys. Res. Lett.,* **35**(12), L12309, doi:10.1029/2008GL033659.

Fialko, Y. 2006. Interseismic strain accumulation and the earthquake potential on the southern San Andreas Fault system, *Nature,* **441**(7096), 968–971.

Funning, G. J., Parsons, B. & Wright, T. J., 2007. Fault slip in the 1997 Manyi, Tibet earthquake from linear elastic modelling of InSAR displacements, *Geophys. J. Int.,* **169**(3), 988–1008.

He, J., Vernant, P., Chéry, J., Wang, W., Lu, S., Ku, W., Xia, W. & Bilham, R., 2013. Nailing down the slip rate of the Altyn Tagh fault, *Geophys. Res. Lett.,* **40**(20), 5382–5386.

Herring, T. A., King, R. W., Floyd, M. A. & McCluskey, S. C., 2016. *Introduction to GAMIT/GLOBK, release 10.6*. Massachusetts Institue of Technology, Available at: http://geoweb.mit.edu/~simon/gtgt/Intro_GG.pdf.

Jolivet, R., Cattin, R., Chamot-Rooke, N., Lasserre, C. & Peltzer, G., 2008. Thin-plate modeling of interseismic deformation and asymmetry across the Altyn Tagh fault zone, *Geophys. Res. Lett.,* **35**(2), L02309, doi:10.1029/2007GL031511.

Le Pichon, X., Kreemer, C. & Chamot-Rooke, N., 2005. Asymmetry in elastic properties and the evolution of large continental strike-slip faults, *J. geophys. Res. Solid Earth,* **110**(B3), B03405, doi:10.1029/2004JB003343.

Li, Y., Shan, X., Qu, C., Liu, Y. & Han, N., 2018. Crustal deformation of the AltynTagh fault based on GPS, *J. geophys. Res. Solid Earth,* **123,** 10309–10322.

Liang, S., Gan, W., Shen, C., Xiao, G., Liu, J., Chen, W., Ding, X. & Zhou, D. 2013. Three-dimensional velocity field of present-day crustal motion of the Tibetan Plateau derived from GPS measurements, *J. geophys. Res. Solid Earth,* **118,** 5722–5732.

Liu, C., Ji, L., Zhu, L. & Zhao, C., 2018. InSAR-constrained interseismic deformation and potential seismogenic asperities on the Altyn Tagh fault at 91.5–95° E Northern Tibetan Plateau, *Remote Sens.,* **10**(6), 943, doi:10.3390/rs10060943.

Loveless, J. P. & Meade, B. J., 2011. Partitioning of localized and diffuse deformation in the Tibetan Plateau from joint inversions of geologic and geodetic observations, *Earth planet. Sci. Lett.,* **303**(1–2), 11–24.

Meade, B. J., Hager, B. H., Mcclusky, S. C., Reilinger, R. E., Ergintav, S., Lenk, O., Barka, A. & Ozener, H., 2002. Estimates of seismic potential in the Marmara Sea region from block models of secular deformation constrained by Global Positioning System measurements, *Bull. seism. Soc. Am.,* **92**(1), 208–215.

Minson, S. E., Simons, M. & Beck, J. L., 2013. Bayesian inversion for finite fault earthquake source models I—theory and algorithm, *Geophys. J. Int.,* **194**(3), 1701–1726.

Molnar, P., Burchfiel, B. C., K'uangyi, L. & Ziyun, Z., 1987. Geomorphic evidence for active faulting in the Altyn Tagh and northern Tibet and qualitative estimates of its contribution to the convergence of India and Eurasia, *Geology,* **15**(3), 249–253.

Molnar, P. & Tapponnier, P., 1975. Cenozoic tectonics of Asia: effects of a continental collision, *Science,* **189,** 419–426.

Nocquet, J. M., 2018. Stochastic static fault slip inversion from geodetic data with non-negativity and bound constraints, *Geophys. J. Int.,* **214**(1), 366–385.

Rosen, P. A., Hensley, S., Peltzer, G. & Simons, M., 2004. Updated repeat orbit interferometry package released, *EOS Trans. Am. geophys. Un.,* **85**(5), 47–47.

Savage, J. C. & Burford, R. O., 1973. Geodetic determination of relative plate motion in central California, *J. geophys. Res.,* **78**(5), 832–845.

Savage, J. C., Gan, W., Prescott, W. H. & Svarc, J. L., 2004. Strain accumulation across the Coast Ranges at the latitude of San Francisco, 1994–2000, *J. geophys. Res.,* **109,** B03413, doi:10.1029/2003JB002612.

Shen, Z. K., Wang, M., Li, Y., Jackson, D. D., Yin, A., Dong, D. & Fang, P., 2001. Crustal deformation along the Altyn Tagh fault system, western China, from GPS, *J. geophys. Res.,* **106,** 30607–30621.

Vernant, P. 2015. What can we learn from 20 years of interseismic GPS measurements across strike-slip faults,. *Tectonophysics,* **644,** 22–39.

Wallace, K., Yin, G. & Bilham, R., 2004. Inescapable slow slip on the Altyn Tagh fault, *Geophys. Res. Lett.,* **31**(9),L09613, doi:10.1029/2004GL019724.

Wang, W., Qiao, X., Yang, S. & Wang, D., 2017. Present-day velocity field and block kinematics of Tibetan Plateau from GPS measurements, *Geophys. J. Int.,* **208**(2), 1088–1102.

Wessel, P., Smith, W. H., Scharroo, R., Luis, J. & Wobbe, F., 2013. Generic mapping tools: improved version released, *EOS Trans. Am. geophys. Un.,* **94**(45), 409–410.

Wright, T. J., Parsons, B., England, P. C. & Fielding, E. J., 2004a. InSAR observations of low slip rates on the major faults of western Tibet, *Science,* **305**(5681), 236–239.

Wright, T. J., Parsons, B. E. & Lu, Z., 2004b. Toward mapping surface deformation in three dimensions using InSAR, *Geophys. Res. Lett.,* **31**(1), L01607, doi:10.1029/2003GL018827.

Xiao, Q., Yu, G., Liu-Zeng, J., Oskin, M. E. & Shao, G., 2017. Structure and geometry of the Aksay restraining double bend along the Altyn Tagh Fault, northern Tibet, imaged using magnetotelluric method, *Geophys. Res. Lett.,* **44**(9), 4090–4097.

Xu, C. & Zhu, S., 2019. Temporal and spatial movement characteristics of the Altyn Tagh fault inferred from 21 years of InSAR observations, *J. Geod.,* **93**(8), 1147–1160.

Zhang, L. *et al.*, 2015. Structure of the Central Altyn Tagh Fault revealed by magnetotelluric data: new insights into the structure of the northern margin of the India-Asia collision, *Earth planet. Sci. Lett.,* **415,** 67–79.

Zhang, P. Z., Molnar, P. & Xu, X., 2007. Late Quaternary and present-day rates of slip along the Altyn Tagh Fault, northern margin of the Tibetan Plateau, *Tectonics,* **26**(5), 1–8.

Zhang, P. Z. *et al.*, 2004. Continuous deformation of the Tibetan Plateau from Global Positioning System data, *Geology,* **32**(9), 809–812.

Zheng, G. *et al.*, 2017. Crustal deformation in the India-Eurasia collision zone from 25 years of GPS measurements, *J. geophys. Res. Solid Earth,* **122**(11), 9290–9312.

Zhu, S., Xu, C., Wen, Y. & Liu, Y., 2016. Interseismic deformation of the Altyn Tagh fault determined by interferometric synthetic aperture radar (InSAR) measurements, *Remote Sens.*, **8**(3), 233, doi:10.3390/rs8030233.

SUPPORTING INFORMATION

Supplementary data are available at *GJI* online.

Figure S1: InSAR and GPS data across the western ATF. All elements are the same as in Fig. 1.
Figure S2: GPS position time-series.
Figure S3: Standard deviations (represented by error bar length) of InSAR data, near the GPS sites, within a radius from 1 to 10 km. Note that, for each radius bin, the *y*-axis of each point has been shifted to 0, so as to highlight its standard deviation. Three GPS stations (AT13, AT14 and AT15, located on the north of the fault), at where the dispersion of the colocated InSAR LOS values is stable and small (RMS < 0.4 mm a^{-1}), are chosen as reference sites to align GPS and InSAR.
Figure S4: Comparison between observed InSAR LOS values (aligned to the GPS reference frame) as a function of observed GPS horizontal velocities projected to LOS. Error bars represent 1σ uncertainties. Dotted line shows the 1:1 line. The four points are distributed around the 1:1 line, implying no obvious relative vertical deformation exist between AT13/AT14/AT15 and AT12.
Figure S5: Fault-parallel and fault-perpendicular components from block rotation. The 0 point on the *x*-axis represents ATF (a) and (b) are the forward model results in the south of the ATF; (c) and (d) are the results in the north of the ATF.
Figure S6: Examples show LOS velocities across the ATF (black points) and curve fitting (red lines) using 'short profile' (left-hand panel) and 'long profile' (right-hand panel). Profile locations are shown in Fig. S1 in the Supporting Information. Note that the InSAR data here have been corrected for the contribution from the Tarim block rotation.
Figure S7: Observed and modelled fault-parallel velocities across the western ATF when all GPS and InSAR data are included in the model. GPS stations are shown in Figs 1 and 3 (upper panel), exclude stations I035, I412 and J343. InSAR data are shown in Fig. 4(a) and are identical to the black dots in Fig. 3 (lower panel). The GPS and InSAR data did not corrected for the contribution from the Tarim block rotation, but are in the same reference frame. Red and blue diamonds with 1σ uncertainty error bars show the fault-parallel velocity component of the GPS and InSAR respectively. Black solid lines represent best fitting curves for (a) GPS data only, (b) InSAR data only. The velocity of each InSAR data point is calculated using the median rates and their standard deviation of all the pixels (gray dots) within a 4-km-wide bin along the profile. The parameters of the best-fitting results are show in each subgraph. Note that positive *d* means dislocation shift to the north.
Figure S8: Different fault slip models and LOS residuals. The upper two panels show two kinds of models. The lower panels show the LOS differences of these two models in different cases; labels in each panel show the slip rates and fault locking depths.
Figure S9: Inversion results using the GPS velocity solution of He *et al*. (2013) and this study. Note the difference of GPS data points in each subpanel.
Figure S10: GPS time-series of the XJQM station and velocity estimate. The upper panel shows the full time-series. The middle panel shows two campaigns, and the lower panel shows three campaigns.
Figure S11: LOS observations (red points) as a function of elevation. Red points in the left-hand panels show InSAR observations, and black points represent the elevation.

Please note: Oxford University Press is not responsible for the content or functionality of any supporting materials supplied by the authors. Any queries (other than missing material) should be directed to the corresponding author for the paper.